Lift-induced vortex dipole collapse

S. Ravichandran,[1,*] Harish N. Dixit,[2,†] and Rama Govindarajan[3,‡]
[1]*TIFR Centre for Interdisciplinary Sciences, Narsingi, Hyderabad 500075, India*
[2]*Department of Mechanical & Aerospace Engineering, IIT Hyderabad, Kandi, Sangareddy 502285, India*
[3]*International Centre for Theoretical Sciences, Shivakote, Bengaluru 560089, India*
(Received 3 August 2016; published 27 March 2017)

Two vortices of opposite sign in two dimensions merely move along parallel lines. We show that even a small buoyancy completely changes this dynamics. When the vortices are of different density from their surroundings, buoyancy produces a lateral drift by Kutta lift. This causes the density patches to merge, and the vortex dipole to collapse. This is followed by a rapid upward (for light vortices) ejection and creation of small-scale structures by baroclinic torque. Our simple analytical equation explains the trajectory of the vortices. We show that these events occur in viscous simulations of many buoyant vortices.

DOI: 10.1103/PhysRevFluids.2.034702

I. INTRODUCTION

Like-signed vortices in two-dimensional flow merge to form larger structures in a process that is well understood (see, e.g., Refs. [1,2]). In contrast, a pair of oppositely signed vortices—a vortex dipole—without gravity simply moves on lines parallel to each other (and perpendicular to the line joining the vortex centers). Our main finding is that vortices which have density patches coincident with them experience, under the action of buoyancy, a Kutta (or Magnus) lift, which causes the vortices to drift laterally. This lateral drift can lead to the collapse of suitably oriented vortex dipoles. In the sequence of events leading to the dipole collapse, the kinetic energy of the system is sacrificed to potential energy. The vortices and density patches are significantly stretched during this process, and this leads to the generation of vorticity at small scales. Solutions from our analytical equation, based on simple physical arguments, agree well with full viscous simulations. This mechanism provides a route for the generation of vorticity at, and hence a cascade of energy to, small scales. We find such dipole collapse events in many-vortex simulations. For simplicity, we restrict our study to two dimensions.

Buoyancy-driven vortical flows are of great significance and have been studied in a variety of situations, most prominently in atmospheric flows [3–5] (see also Ref. [6] and references therein, and Ref. [7] and references therein in the context of vortex rings). Such vortex rings are encountered in the ringlike patterns following a nuclear explosion. Turner [4], from inviscid theory and experiments, showed that light vortex rings expand in their radius. Buoyant vortices also have an important application in the formation of large-scale cloud systems in the atmosphere [8]. Plumes and thermals aided by turbulent convection transport lighter density fluid to high altitudes [6]. In clouds, buoyant vortices can also arise from the effects of particle inertia [9]. Water droplets, which act as nuclei for condensation of vapor, are centrifuged out of regions of vorticity, leaving voids where no phase change occurs. Since condensation and the resultant latent heating occur only outside vortical regions, the region outside the vortices is heated up, leaving the vortices colder (and denser) than their surroundings. For a recent historical review of the relevance of such fluid dynamic phenomena to cloud physics, see Yano [10]. The major body of earlier work has been on isolated buoyant vortices, but our primary interest is in the interaction between vortices. Our findings have significance for all the flows discussed.

*ravis@tifrh.res.in
†hdixit@iith.ac.in
‡rama@icts.res.in

A study of vortex dipoles in stratified environments was carried out by Garten *et al.* [11]. They find that the collapse of the dipole occurs because of countersigned vorticity at the edge of the original vortices created because of baroclinic torque. In contrast, we have no background stratification and find little or no countersigned vorticity at the edges of our vortices until the late stages of the dynamics. Since we do not add noise to the system, we also do not find the oscillations of the direction of propagation of the dipole reported by Garten *et al.*

Counter-rotating vortices in the absence of buoyancy are known, in three dimensions, to undergo a cut-and-connect instability to form vortex rings [12]. Our study, since it is two-dimensional, excludes this possibility. A three-dimensional study where the present mechanism and the cut-and-reconnect mechanism are in competition would be of interest.

In the following, we use "merger" and "collapse" interchangeably with the understanding that they refer to the process in which the density patches associated with the vortex dipoles merge, whereas the vorticity associated with the dipole is erased via the action of baroclinic torque.

II. LIFT ON BUOYANT VORTICES

Consider a two-dimensional vortex of circulation $\mathbf{\Gamma}$, located in a concentric circular patch of fluid that is different in density from its surroundings, in a gravitational field. The Reynolds number for such a vortex, given by $\mathrm{Re} = \Gamma/\nu$, is usually high. We therefore assume that vorticity does not diffuse significantly during the time of evolution of the dynamics, and our viscous simulations bear out this assumption. The density difference gives rise to a buoyancy force, causing a light vortex to rise vertically upwards with a velocity $\mathbf{v}$ relative to the surrounding fluid. In our simplified theory we model the vortex as a rotating cylinder, which by the Kutta-Joukowski theorem [13] experiences a lift force (Magnus force) per unit normal length given by

$$\mathbf{f}_L = \rho_0(\mathbf{\Gamma} \times \mathbf{v}). \tag{1}$$

We know that spinning solid bodies can, under the action of the Magnus force, execute complicated trajectories [14,15]. This lift exists because of the relative velocity $\mathbf{v}$ between the bodies and the fluid. We find that the density difference between a vortex and its surroundings, in a gravitational field, is necessary (and sufficient) for $\mathbf{v}$ to be nonzero and for the generation therefore of Kutta lift. The density difference can be characterized by an Atwood number, $A = (\rho_0 - \rho_i)/\rho_0$, the density of the core being $\rho_i = \rho_0(1 - A)$ where ρ_0 is the density of the surroundings. Under the Boussinesq approximation, light- and heavy-cored vortices behave in mirror-opposite ways: The potential energy of light-cored vortices increases as they are pushed downwards (since buoyancy tries to push them upwards) and vice versa for a heavy-cored vortex. This is also true for the lift on the vortices, since the relative velocity $\mathbf{v}$ in Eq. (1) will have opposite signs for light- and heavy-cored vortices. This can also be seen by looking at the equation for the vorticity in Eqs. (6) and noting that the signs of both the buoyancy and the vorticity have to be reversed for the equation to remain unchanged.

We now consider a vortex dipole and define its orientation as the direction in which the dipole would move in the absence of buoyancy. For the vortex dipole to collapse under the action of lift, it has to be oriented such that its potential energy tends to increase initially. With no loss of generality, therefore, we consider the case where the core is lighter. The vortex experiences a buoyancy force (per unit length) given by

$$\mathbf{f}_g = g\rho_0 A \Delta \hat{j}, \tag{2}$$

where g is acceleration due to gravity, Δ is the area of the compact vortex, and $\hat{j}$ is the unit vector in the vertical direction. For a Rankine vortex of diameter d_0 and vorticity ω_0 inside a core of area $\Delta = \pi d_0^2/4$, we have $\mathbf{\Gamma} = \omega_0 \Delta \hat{k}$, where $\hat{k}$ is a unit vector along the axis of the vortex. Introducing a drag proportional to the square of the relative velocity of the vortex and the surrounding fluid, and nondimensionalizing the above equation using the length and time scales, $L = d_0$ and $T = 1/\omega_0$,

the equation of motion of the vortex centroid can be written as

$$\frac{d\mathbf{v}}{dt} = \frac{\mathrm{Fr}^{-2}}{1-A}\hat{j} + \frac{\hat{k}\times\mathbf{v}}{(1-A)} - \beta d_0|\mathbf{v}|\mathbf{v}, \tag{3}$$

where β is the drag coefficient and $\mathrm{Fr}^2 = \omega_0^2 L/gA$ is the square of the Froude number. We only consider the inviscid case, $\beta = 0$, here. Equation (3) can be integrated for a single vortex to give, for the horizontal and vertical components of velocity respectively,

$$\begin{aligned} v_x = \frac{dx}{dt} &= -\frac{1}{\mathrm{Fr}^2} + \left[v_x^0 + \frac{1}{\mathrm{Fr}^2}\right]\cos\left[\frac{t}{1-A}\right] - v_y^0 \sin\left[\frac{t}{1-A}\right], \\ v_y = \frac{dy}{dt} &= v_y^0\cos\left[\frac{t}{1-A}\right] + \left[v_x^0 + \frac{1}{\mathrm{Fr}^2}\right]\sin\left[\frac{t}{1-A}\right], \end{aligned} \tag{4}$$

where the superscript 0 refers to an initial condition. This gives an oscillatory solution in general and has the equilibrium solution

$$v_x = -\frac{1}{\mathrm{Fr}^2}, \quad v_y = 0, \tag{5}$$

for suitably chosen initial conditions. Upon integrating Eq. (4) it is clear that a vortex with $\omega_0 > 0$ will move leftwards linearly in time with a speed inversely proportional to Fr^2, with its trajectory modulated by an oscillation at frequency $(1-A)^{-1}$. The direction of motion is reversed if the sign of vorticity is changed. Therefore, two appropriately located opposite-signed vortices will move towards and collide with each other. In turbulence, vortices are closer to Lamb-Oseen than to Rankine, but the idealized inviscid theory, with no fitting parameters, is able to reproduce the behavior of a buoyant vortex, as seen below.

III. DIRECT NUMERICAL SIMULATIONS OF LIGHT GAUSSIAN VORTICES

We now test the model against direct numerical simulations (DNS) of the two-dimensional Navier-Stokes and scalar density Eqs. (6) below:

$$\begin{aligned} \frac{\partial\omega}{\partial t} + \boldsymbol{u}\cdot\nabla\omega &= \frac{1}{\mathrm{Re}}\nabla^2\omega + \frac{\partial B}{\partial x}, \\ \frac{\partial\rho}{\partial t} + \boldsymbol{u}\cdot\nabla\rho &= \frac{1}{\mathrm{Re}\cdot\mathrm{Pr}}\nabla^2\rho, \\ B &= \frac{1}{\mathrm{Fr}^2}\frac{(\rho_0-\rho)}{\rho_0}, \\ \nabla^2\psi &= -\omega, \\ u &= \frac{\partial\psi}{\partial y}, \\ v &= -\frac{\partial\psi}{\partial x}. \end{aligned} \tag{6}$$

We start with Gaussian vortices and density patches. The simulations are done with a Fourier pseudospectral method with 1024^2 (for the two-vortex cases) or 4096^2 (for the many-vortex simulations) collocation points with an SSPRK3 scheme for the advection terms combined with a Crank-Nicolson scheme for the viscous terms. The code has been validated against Ref. [16]. The Reynolds and Froude numbers of the simulation are given by

$$\mathrm{Re} = \frac{\Omega_0 d_0^2}{\nu}, \quad \mathrm{Fr}^2 = \frac{\Omega_0^2 d_0}{gA}, \tag{7}$$

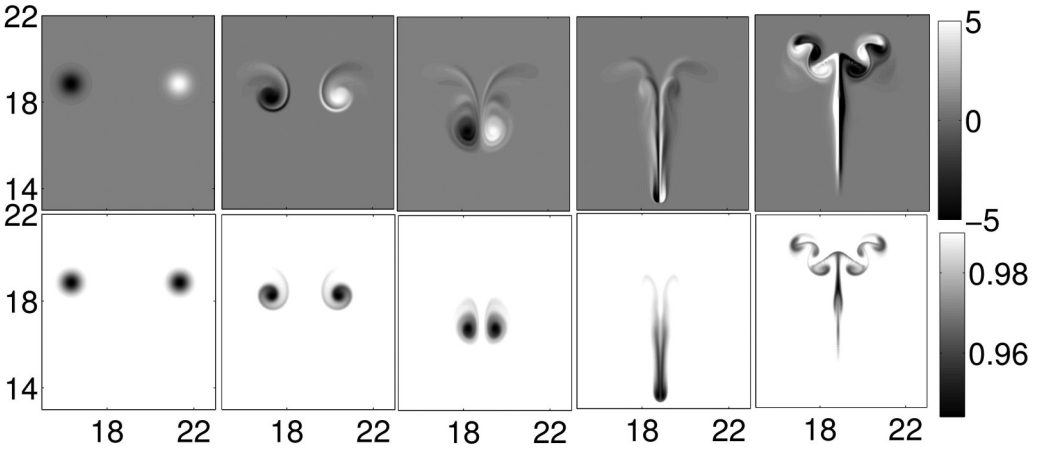

FIG. 1. The sequence in the collapse of a vortex dipole with lighter patches. Top: vorticity contours; bottom: density contours. The vortices move downwards and towards each other. Their density patches merge when the potential energy is at a maximum (height is lowest). A strong upward thrust follows, with baroclinic vorticity produced opposite from the original. The dimensional time t^* left to right is 0,5,10,15, and 20; Re = 5000; and $\mathrm{Fr}^2 = 25$.

where Ω_0 is the peak vorticity, d_0 is the characteristic radius of the Gaussian vortices, and ν is the kinematic viscosity. For all our simulations, we use $A = 0.1$. Note that, unless explicitly stated otherwise, we report results from our simulations in dimensional units (i.e., $\Omega_0 \neq 1$ in Fig. 1, for instance).

We notice in Eq. (4) that a vortex with an initially stationary centroid at large Froude number will oscillate with an amplitude much smaller than its radius, and in a viscous simulation of a Gaussian vortex we expect to observe only a steady leftward motion. In fact we find that the mean leftward velocity is independent of the Reynolds number for a wide range of Reynolds numbers, in agreement with Eq. (4). This is shown in Fig. 3. However, we do not capture the oscillation frequency in our simulations; this is in part because of the ambiguity associated with defining a center for the vortices (which no longer maintain a circular shape).

IV. ANNIHILATION OF VORTEX DIPOLES

Figures 1 and 2 show pictures from a simulation of a vortex dipole (a movie showing the merger in slow motion is included in the Supplemental Material [17]). The Biot-Savart velocities induced by the vortices on each other point downwards, and the dipole moves downwards initially. As the dipole carries the light patches downwards with it, the system gains in potential energy, with a corresponding loss in kinetic energy. The vortices in the dipole are "lifted" towards each other, retaining, for $\mathrm{Fr}^2 \geqslant 25$, a more or less circular shape. Deviations from circularity, for relatively low Fr^2, take the form of spiral arms of vorticity around the parent vortices. Since the density patches are also deformed, baroclinic torques lead to the creation of a small amount of countersigned vorticity near the spiral arms. These spiral arms have vorticity of the same sign as the parent vortices and are eventually reabsorbed into the parent vortices, becoming penumbral regions around the parent vortices.

As the vortices come closer to each other, they accelerate and the vorticity in penumbral regions is detrained first. The vortices (and the density patches) are also significantly stretched, massively increasing the baroclinic production of vorticity (of both signs). This happens both in the vicinity of the vortex dipole and in the detrained regions. The gradients of density are steepest in the region between the two vortices, where the vorticity produced is of the same sign are the parent vortices. The gradients on the outer edges of the vortices are shallower and start acting much later ($t = 15$), producing countersigned vorticity. The system of vortex dipole and the detrained regions now

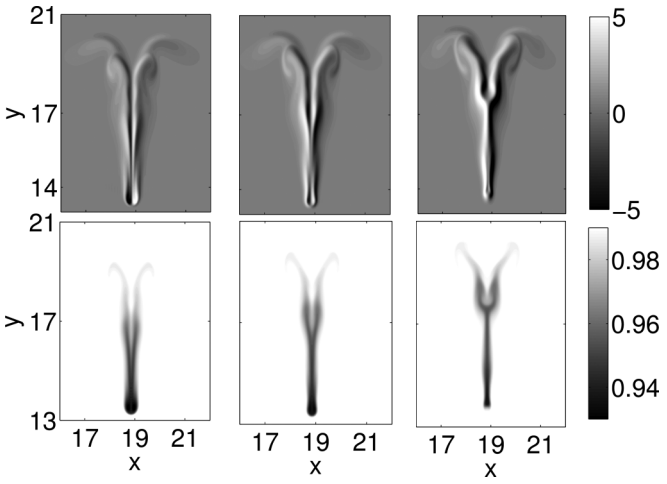

FIG. 2. The sequence of events leading to the collapse of the vortex dipole. Top: vorticity contours; bottom: density contours. The (dimensional) time from left to right is 15.5, 16.5, and 17.5. First, as the vortices near each other, they are stretched vertically, and the detrained tail almost separates from the dipole ($t^* = 15.5$, left). Then, as the parent vortices are shrunk by the action of baroclinic torque, the downward motion is arrested ($t^* = 16.5$, middle). And finally, as the dipole begins to move upwards, the vortices are erased entirely ($t^* = 17.5$, right).

resembles a tadpole. The tail of this tadpole is made up of vorticity and density detrained from the vortex dipole. The vorticity produced in the tail region causes the tail to detach from the vortex dipole.

The density patches of the vortex dipole merge at around $t = 15.5$ and the baroclinic term vanishes in the region between the vortices. On the outside, however, the baroclinic term continues to erase the vorticity of the parent vortices, until they are so weak that the dipole comes to rest and starts to move upwards against Biot-Savart ($t = 16$–16.5). This happens before the vortices disappear entirely. At this point, there are two tails in each half of the domain: one tail, of the same sign as

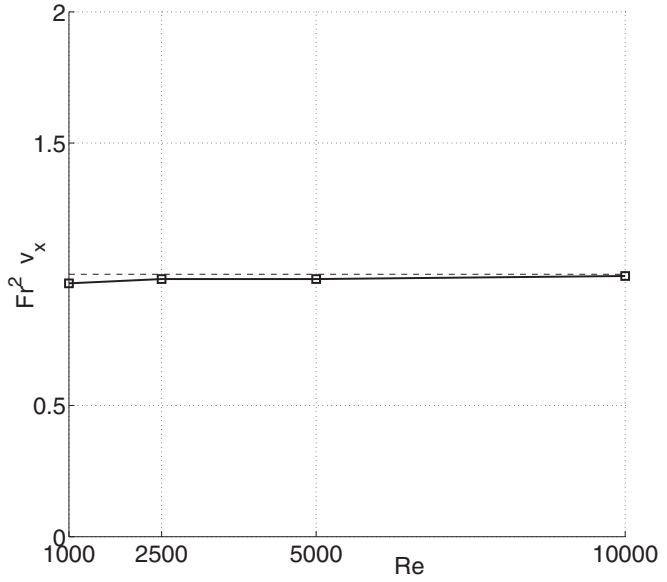

FIG. 3. The leftward velocity of a single vortex matches the theoretical value of $1/\mathrm{Fr}^2$ and is independent of the Reynolds number for a wide range of Reynolds numbers.

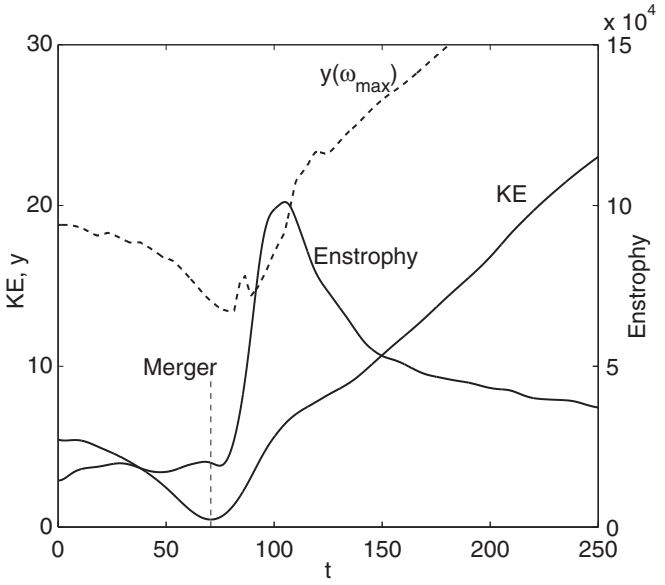

FIG. 4. The total enstrophy and the kinetic energy explode after the vortices come together. Here Re $= 5000$, $\mathrm{Fr}^2 = 25$. The merger time is taken to be the time at which the kinetic energy reaches a minimum.

the parent vortex from which it was detrained, and another caused by baroclinic production. The baroclinically produced tail is further away from the center. As the dynamics proceed, the tails bunch up into separate vortices which then pair up.

Figure 4 shows that the enstrophy increases dramatically after the merger (denoted by the vertical dashed line plotted at the time at which the kinetic energy reaches a minimum). A smoothed plot of the location of the maximum vorticity (the dashed line) shows that the vortices reach their minimum height at around the same time as the kinetic energy reaches a minimum. The blip in the position of maximum vorticity around the merger occurs because of the annihilation of vorticity around the merging density patches. We note that the dynamics of buoyant vortex dipoles is distinct from that of unlike-signed line vortices of constant density perturbed sinusoidally, where the vortices reconnect [12].

The trajectories predicted from our idealized equations capture the motion of vortices very well whether or not there is a left-right symmetry, as seen in Fig. 5, only failing when the vortices come very close to each other and are significantly distorted. The analytical prediction is much better for the larger of the Froude numbers since the vortices are less prone to distortion and because the baroclinic torque production is lower.

We may define a merger time t_{merger} as the time at which the density patches overlap, and the kinetic energy is at its minimum (Appendix A provides an explanation of why the two times coincide). We use this definition for both inviscid and viscous simulations. If the vortices are assumed to approach each other at the velocity given by (5), a simple scaling argument gives

$$t_{\mathrm{scaling}} = \frac{\Delta x^0}{2v_x} = \frac{\Delta x^0 \cdot \mathrm{Fr}^2}{2}, \tag{8}$$

if the vortices start a distance Δx^0 apart. Figure 6 shows that merger times found by numerically integrating Eqs. (3) agree almost exactly with the scaling relationship in Eq. (8) for symmetric initial conditions. Merger times from viscous simulations are slightly longer than the scaling relationship predicts, since the vortices are significantly distorted as they come close to each other. In realistic simulations, asymmetric initial conditions would be more relevant. Merger times are unchanged for

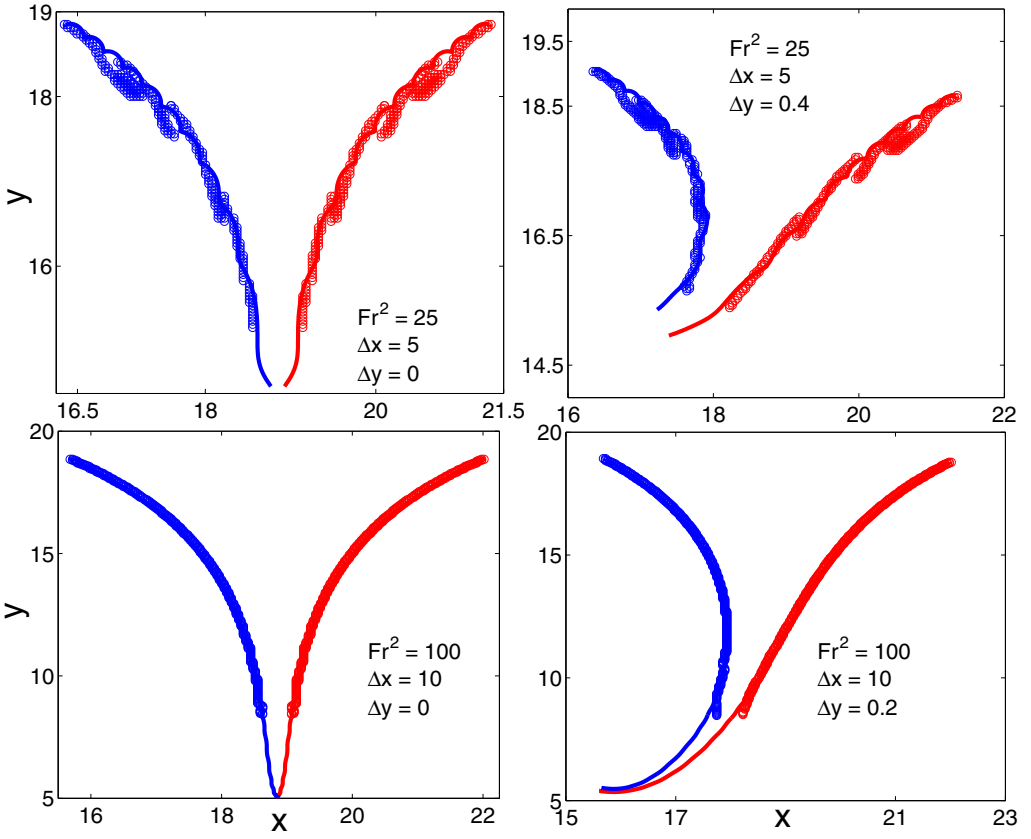

FIG. 5. Comparison of the time trajectory of the maximum vorticity between idealized theory (solid lines) and simulations (symbols). At higher gravity (lower Fr), the maximum vorticity can be in the filaments of baroclinic vorticity rather than at the original vortex, so systematic deviations are seen from the theory.

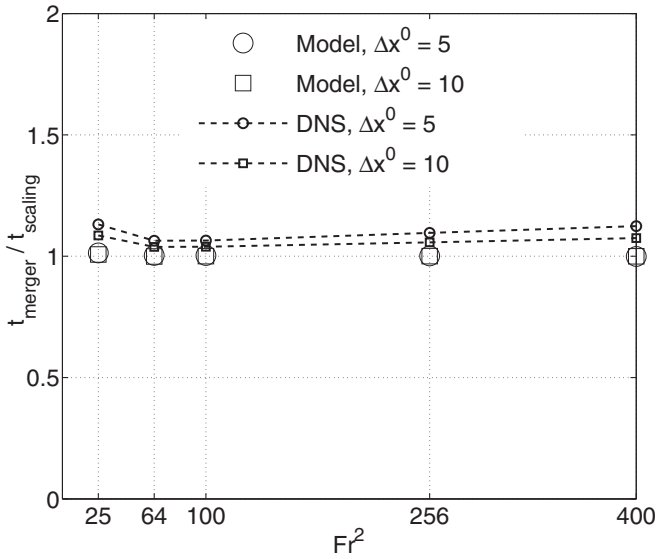

FIG. 6. Dependence of t_{merger} on the Froude number.

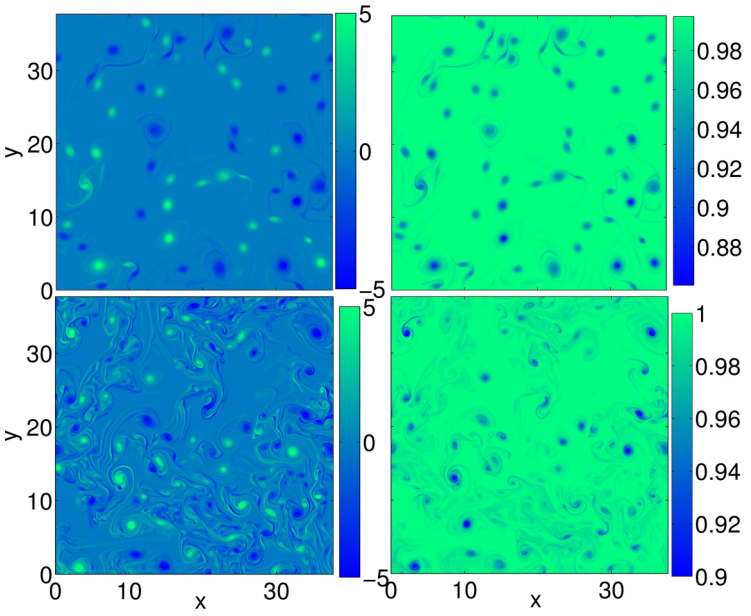

FIG. 7. The state, at $t = 25$, of evolution of a system of vortices in a periodic box (with $\mathrm{Re} = 5000$, $\mathrm{Fr}^2 = 25$ based on the strength of a single vortex). The vortices are initially of identical strengths, and equal numbers are positive and negative. Top row: system with no buoyancy; bottom row: with buoyancy. Left: vorticity; right: density.

the asymmetric initial configurations shown in the right panels of Fig. 5, but the maximum kinetic energy and enstrophy after merger are smaller (as can be seen in Fig. 14 in Appendix B).

V. DNS OF MANY VORTICES IN A PERIODIC BOX

We now ask whether the effect of gravity on light vortices will affect turbulent flow. We perform a simulation with 100 Gaussian vortices of the same strength (equally distributed between positive

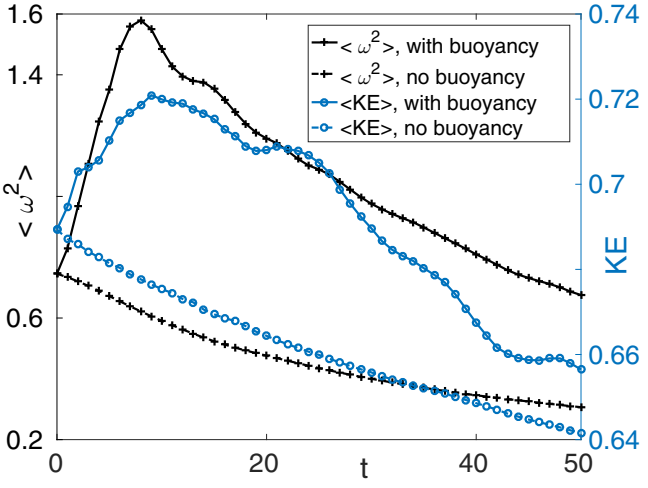

FIG. 8. Enstrophy (left axis, black) and kinetic energy (right axis, blue online) evolution for the many-vortex simulations, with (solid lines) and without (dashed lines) buoyancy.

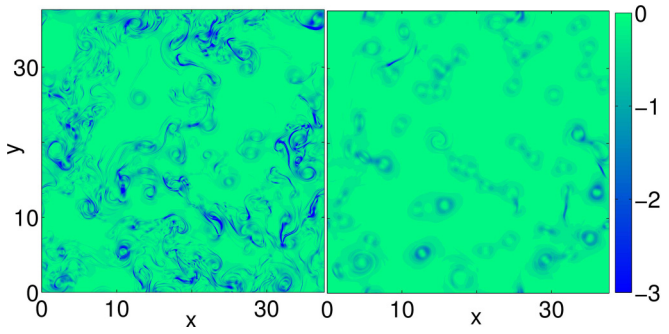

FIG. 9. The determinant of the strain matrix for simulations (with 4096^2 points) with many vortices in a periodic box. Left: with buoyancy; right: no buoyancy. The figures are plotted for $t = 20$.

and negative) placed randomly initially in a periodic box of side 12π. We allow for the vortices to overlap. The Reynolds number based on the circulation of one vortex is 5000, $A = 0.1$, and $\mathrm{Fr}^2 = 25$. For contrast, we run simulations with gravity switched off. Here, the density patches act merely as passive scalars, with no buoyancy effects.

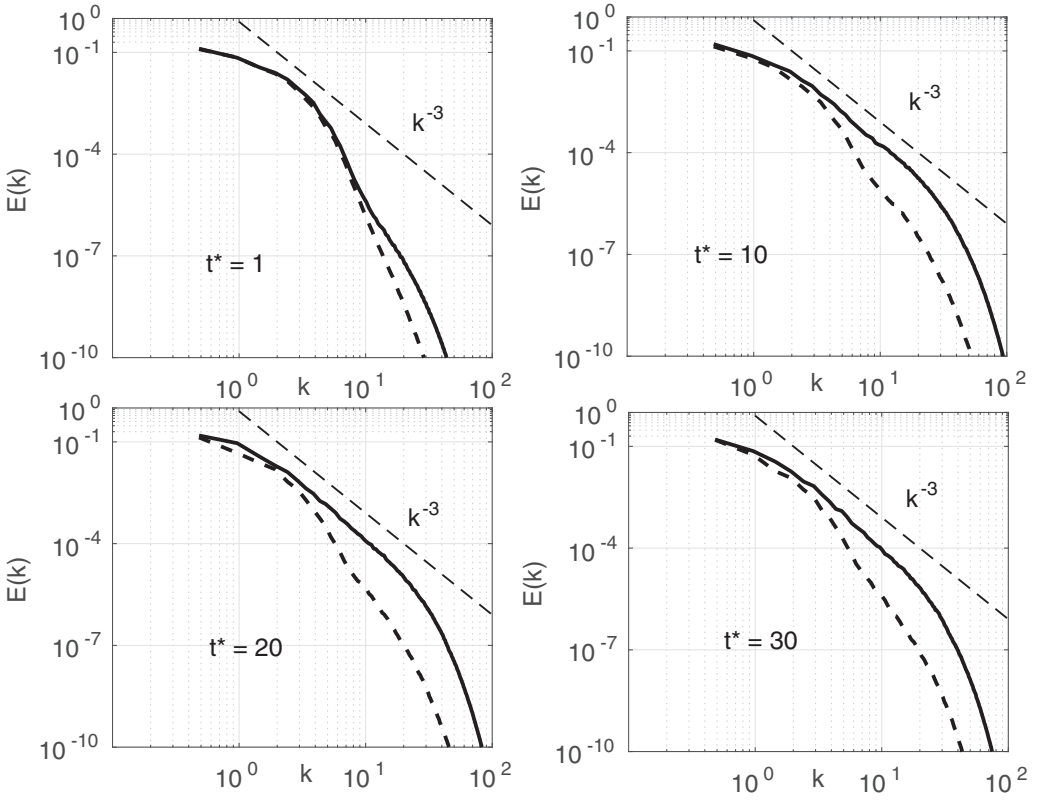

FIG. 10. KE spectrum for simulations with many vortices in a periodic box. The kinetic energy spectra at different times (dimensional time $t^* = 1,10,20,30$) for simulations with and without buoyancy. We use 1000 bins to plot the spectra. The spectra with buoyancy effects (solid lines) included are much fuller than the spectra without buoyancy effects (dashed lines) and closer to k^{-3} scaling shown in the figures.

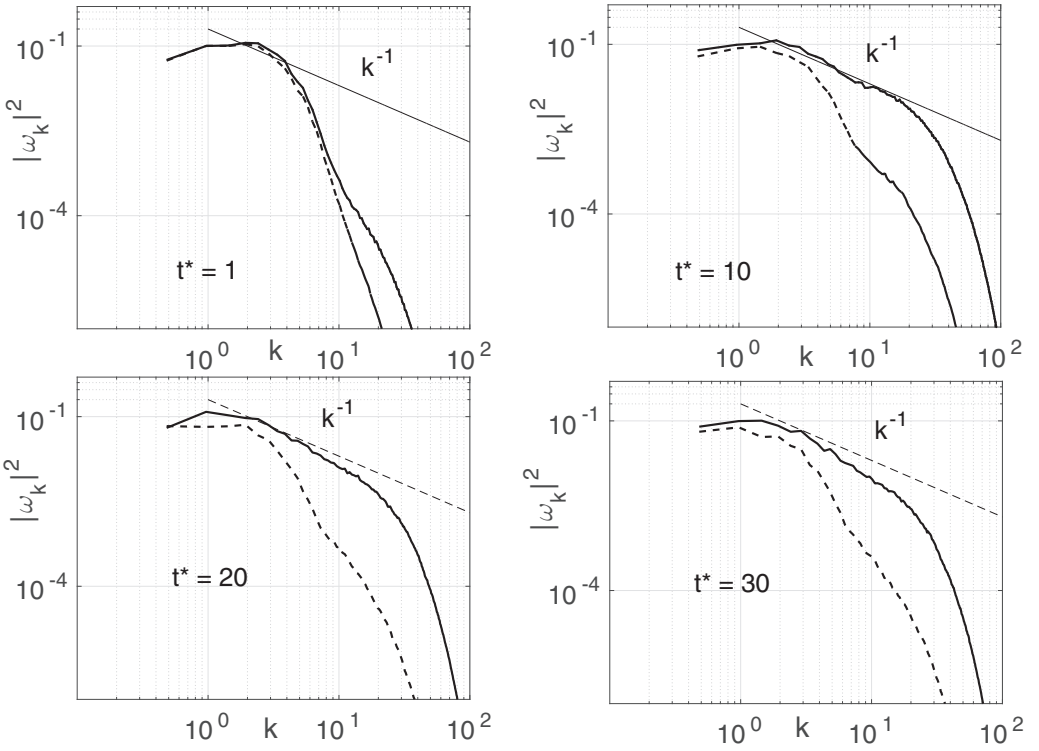

FIG. 11. Enstrophy spectra for simulations with many vortices in a periodic box, showing that the spectra with buoyancy effects (solid lines) included are much fuller than the spectra without buoyancy effects (dashed lines), and closer to k^{-1} scaling shown in the figures. The same procedure as in Fig. 10 is followed.

Figure 7 shows the state of the two systems at $t = 25$. The movie in the Supplemental Material [17] shows several collision events (see Appendix C) which create small-scale structures and lead to the initial steep rise in enstrophy and kinetic energy seen in Fig. 8. Note that not all small-scale structures are caused by vortex collisions.

The message of Fig. 7 is reiterated strongly in Fig. 9 where we plot the determinants of the strain matrix for simulations with and without buoyancy. The significantly higher values of $\det(S)$ for the buoyant case directly quantify the effects of buoyancy. It is evident that baroclinic torque significantly stretches and distorts buoyant vortices.

Finally, we plot the kinetic energy and enstrophy spectra. Figures 10 and 11 show the kinetic energy and enstrophy spectra, respectively, for simulations with and without buoyancy. We see that the higher wave numbers have significantly higher contributions in the simulations with buoyancy, showing that buoyancy induces a forward cascade. This can be explicitly seen in Fig. 12 where the kinetic energy fluxes in spectral space are plotted for simulations with and without buoyancy. The flux for the case with buoyancy is positive for $k > 10$, showing that energy is transferred from large to small scales. We also note from the figures that the simulations with buoyancy behave more like fully developed stationary turbulence (i.e., $E(k) \sim k^{-3}$) than the simulations without buoyancy. This is to be expected, since our system is not forced except for the contributions of buoyancy. The time at which the spectra look like fully developed turbulence is of the same order as the time at which the kinetic energy and enstrophy in the system peak (see Fig. 8).

In summary, our theory and simulations show that even low levels of buoyancy can greatly influence vortex dynamics and turbulence. In our dramatic example, Kutta lift, acting as a Magnus force, propels two opposite-signed vortices towards each other, leading to their collision and the

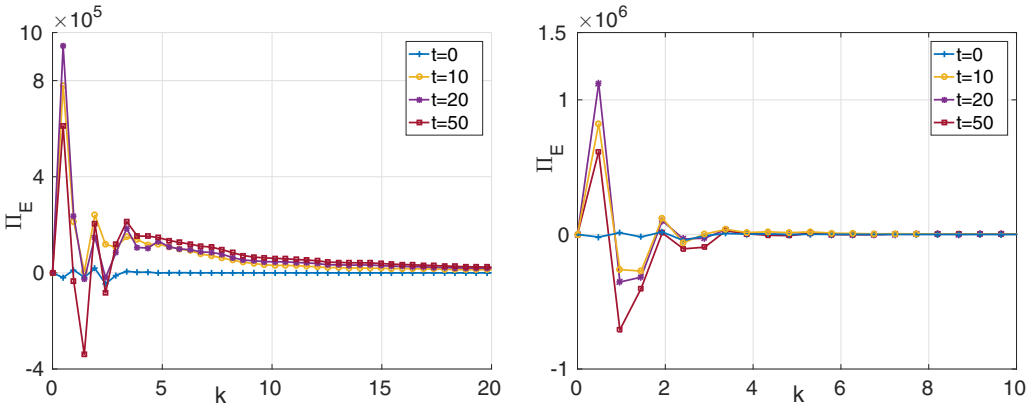

FIG. 12. Energy fluxes in spectral space for the simulations of many vortices in a periodic box. The flux is positive for the case with buoyancy, showing a forward cascade of energy to smaller scales.

merger of their density cores. During this part of the process, the system moves downwards, sacrificing kinetic energy for potential energy. This is followed by rapid upward motion, associated with high strain and energetic small scales, as revealed by the kinetic energy spectrum.

APPENDIX A: CALCULATION OF t_{merger}

In the paper, we calculate t_{merger}, the merger time for a pair of unlike-signed vortices, by looking for when the kinetic energy of the system—as measured by summing $\frac{1}{2}(u^2 + v^2)$ over all grid points in DNS or by calculating the Biot-Savart induced velocities from the two vortices on a grid of points in the analytical simulations—reaches a minimum. We now justify this choice. Figure 13(a) shows that the kinetic energy is an excellent measure of when the vortices "collide" in model simulations. Figure 13(b) shows that kinetic energy calculated from the model compares well with the kinetic energy calculated from DNS until merger, with the caveat that the kinetic energy in DNS does not

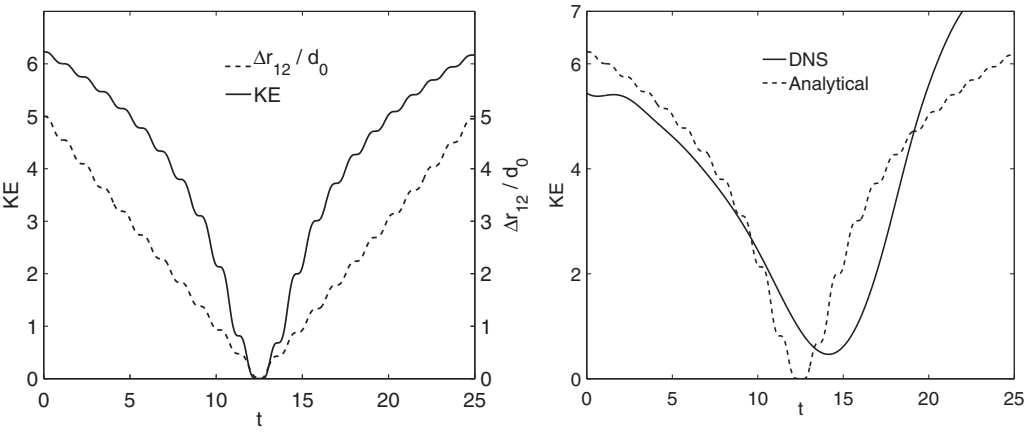

FIG. 13. The kinetic energy (calculated as described in the text) for a pair of unlike-signed vortices with $\text{Re} = 5000$ and $\text{Fr}^2 = 25$. The figure on the left shows for simulations of the model equation (3) (with $\beta = 0$) the variation of the kinetic energy and the separation between the vortex centroids. The figure on the right shows how the kinetic energies in model simulations and DNS compare with each other.

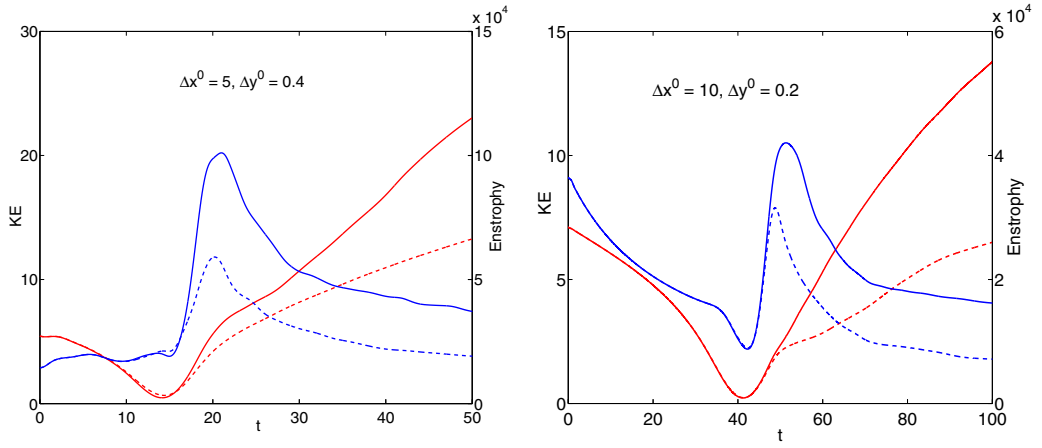

FIG. 14. Plots of kinetic energy (left axis, red curves) and enstrophy (right axis, blue curves) for the asymmetric conditions(dashed curves) compared with the symmetric conditions (solid curves) from Fig. 3. The dotted lines are plots for the asymmetric conditions. Δx^0 and Δy^0 are the initial separations between the vortices ($\Delta y^0 = 0$ for the symmetric initial condition). Left: Re $= 5000$ and $\mathrm{Fr}^2 = 25$; right: Re $= 5000$, $\mathrm{Fr}^2 = 100$.

go to zero. Note also that, in the model, the rise of the kinetic energy after collision is symmetric to its fall before collision; this is not true in DNS.

APPENDIX B: ASYMMETRIC INITIAL CONDITIONS

Figure 3 shows vortex collisions with (left-right) symmetric and asymmetric initial conditions. In the asymmetric initial conditions, the two vortices are not at the same horizontal level. The model developed in our work captures the behavior of vortices even in these conditions. Not all such pairs of vortices will collide, of course. Two vortices that are too far separated in the y direction are unlikely to collide. They will instead just come close to each other before sling-shotting past each other. In the cases where vortices do collide, the collision times t_{merger} are about the same as for the symmetric case. This is seen in Fig. 14. Note also that the maximum enstrophy produced is markedly higher for the symmetric initial condition, showing that not all unlike vortex collisions are created equal.

APPENDIX C: INCLUDED MOVIES

1. Vortex-dipole collapse

The slow-motion movie ("slow_motion_Re5000_Fr25.avi") included in the Supplemental Material [17] shows in detail how the opposite-signed vortices collide and the density patches associated with them merge. As the vortices come closer to each other, they are stretched and distorted, eventually leaving behind them *comet-tail*-like trails of lower density. The vorticity around the main density patches is all but annihilated under the action of baroclinic torque, allowing the density patches to merge and come to rest. As this is happening, the comet tails of lower density have generated their own vorticity of opposite sign to what they were initially associated with. Finally, as the entire system begins to rise, the combined density patch shoots upwards to overtake the density tails.

2. Many-vortex simulations

The movies ('light_manyvor.avi' and 'nobuoy_manyvor.avi') included in the Supplemental Material [17] show the dynamics of 100 vortices. The simulations were started with identical

initial conditions, except that one simulation had buoyancy switched off. The patches of density act merely as a passive scalar in the no-buoyancy simulations. Several collision events can still be seen in the movie of the buoyant vortices. For instance, at $t = 2$, the following (x, y) locations have collisions occurring near them: (i) $x = 0, y = 30$, (ii) $x = 20, y = 30$, (iii) $x = 32, y = 32$, and (iv) $x = 5, y = 5$. Note that some of these are collisions between more than one vortex, a possibility we have not discussed in the paper.

---

[1] G. Boffetta and R. E. Ecke, Two-dimensional turbulence, Annu. Rev. Fluid Mech. **44**, 427 (2012).

[2] C. Cerretelli and C. H. K. Williamson, The physical mechanism for vortex merging, J. Fluid Mech. **475**, 41 (2003).

[3] R. S. Scorer, Experiments on convection of isolated masses of buoyant fluid, J. Fluid Mech. **2**, 583 (1957).

[4] J. S. Turner, Buoyant vortex rings, Proc. R. Soc. London, Ser. A **239**, 61 (1961).

[5] A. Shapiro and K. M. Kanak, Vortex formation in ellipsoidal thermal bubbles, J. Atmos. Sci. **59**, 2253 (2002).

[6] J. S. Turner, Buoyant plumes and thermals, Annu. Rev. Fluid Mech. **1**, 29 (1969).

[7] K. Shariff and A. Leonard, Vortex rings, Annu. Rev. Fluid Mech. **24**, 235 (1992).

[8] S. C. Sherwood, D. Hernandez-Deckers, and M. Colin, Slippery thermals and the cumulus entrainment paradox, J. Atmos. Sci. **70**, 2426 (2013).

[9] R. A. Shaw, W. C. Reade, L. R. Collins, and J. Verlinde, Preferential concentration of cloud droplets by turbulence: Effects on the early evolution of cumulus cloud droplet spectra, J. Atmos. Sci. **55**, 1965 (1998).

[10] J.-I. Yano, Basic convective element: Bubble or plume? A historical review, Atmos. Chem. Phys. **14**, 7019 (2014).

[11] J. F. Garten *et al.*, Dynamics of counter-rotating vortex pairs in stratified and sheared environments, J. Fluid Mech. **361**, 189 (1998).

[12] M. V. Melander and F. Hussain, Cut-and-connect of two antiparallel vortex tubes, in *Studying Turbulence Using Numerical Simulation Databases*, Proceedings of the 1988 Summer Program (Stanford University, Stanford, CA, 1988), pp. 257–286.

[13] J. D. Anderson Jr., *Fundamentals of Aerodynamics* (McGraw-Hill Higher Education, New York, 2011).

[14] G. Dupeux, A. Le Goff, D. Quéré, and C. Clanet, The spinning ball spiral, New J. Phys. **12**, 093004 (2010).

[15] G. Dupeux, C. Cohen, A. Le Goff, D. Quéré, and C. Clanet, Football curves, J. Fluids Struct. **27**, 659 (2011).

[16] H. N. Dixit and R. Govindarajan, Vortex-induced instabilities and accelerated collapse due to inertial effects of density stratification, J. Fluid Mech. **646**, 415 (2010).

[17] See Supplemental Material at http://link.aps.org/supplemental/10.1103/PhysRevFluids.2.034702 for movies showing the annihilation of countersigned vortices.